Article

Not peer-reviewed version

# Effective and Enduring Electric Vehicle Heat Pump Enhanced by Microchannel Heat Exchanger with Superhydrophobic Surface Treatment

Yunren Sui , Zengguang Sui , Guangda Liang , Wei Wu *

Posted Date: 4 August 2023

doi: 10.20944/preprints202308.0414.v1

Keywords: superhydrophobic surface treatment; electric vehicle; heat pump; microchannel heat exchanger; coefficient of performance

*Article*

# Effective and Enduring Electric Vehicle Heat Pump Enhanced by Microchannel Heat Exchanger with Superhydrophobic Surface Treatment

**Yunren Sui [1,2,†], Zengguang Sui [1,2,†], Guangda Liang [1,2] and Wei Wu [1,2,*]**

[1] School of Energy and Environment, City University of Hong Kong, Hong Kong, China
[2] Shenzhen Research Institute, City University of Hong Kong, Shenzhen, China
* Correspondence: weiwu53@cityu.edu.hk
† **Yunren Sui** and **Zengguang Sui** contributed equally to this manuscript.

**Abstract:** Battery-powered electric vehicles (EVs) have emerged as an environmentally friendly and efficient alternative to traditional internal combustion engine vehicles, while their single-charge driving distances under cold conditions are significantly limited due to the high energy consumption of heating systems. Heat pumps can provide an effective heating solution for EVs, but their coefficient of performance (COP) is hampered by heat transfer deterioration due to frost accumulation. This study proposes a solution to this issue by introducing a microchannel heat exchanger (MHE) with superhydrophobic surface treatment (SHST) as a heat pump evaporator. A computational-fluid-dynamics MHE model and a dynamic heat pump model are developed and rigorously validated to examine the detrimental impact of frost accumulation on heat transfer, airflow resistance, and heat pump performance. When the frost layer thickness is 0.8 mm at a given air-side velocity of 1.0 m/s, the air-side heat transfer coefficient can be reduced by about 75%, and the air-side pressure drop sharply increases by 28.4 times. As frost thickness increases from 0 to 0.8 mm, the heating effect drops from 3.97 to 1.82 kW, and the system COP declines from 3.17 to 2.30. Experimental results show that the frost thickness of the MHE with SHST reaches approximately 0.4 mm after 30 minutes, compared to that of 0.8 mm of the MHE without SHST, illustrating the defrosting capability of the superhydrophobic coating. The study concludes by comparing the performance of various heating methods in EVs to highlight the advantages of SHST technology. As compared to traditional heat pumps, the power consumption of the proposed system is reduced by 48.7% due to the defrosting capability of the SHST. Moreover, the single-charge driving distance is extended to 327.27 km, an improvement of 8.99% over the heat pump without SHST.

**Keywords:** superhydrophobic surface treatment; electric vehicle; heat pump; microchannel heat exchanger; coefficient of performance

## 1. Introduction

Amid the global shift towards carbon neutrality, battery-powered electric vehicles (EVs) have emerged as an environmentally friendly and efficient alternative to traditional internal combustion engine vehicles, attracting significant attention in recent years [1,2]. For EVs reliant entirely on battery power, the air conditioning system is the second most energy-intensive component after the powertrain, consuming about a third of the total energy supplied by the battery [3]. Therefore, it plays a critical role in improving energy efficiency and thermal comfort in EVs [4]. The energy sources for air conditioning systems differ between electric and fuel vehicles. Fuel vehicles use the engine to drive the air conditioning compressor for cooling and exploit waste heat for heating and defrosting. However, EVs do not have the benefit of engine waste heat [5]. As a result, the energy needed for cooling, heating, and defrosting in EVs comes solely from the battery, significantly decreasing the single-charge driving distance.

Under severe winter conditions, the heat pump system is an effective alternative for EV heating to traditional positive temperature coefficient (PTC) heating due its high coefficient of performance (COP). Contrary to the cooling process where the condenser is inside, the heating process uses an indoor condenser and an outdoor evaporator [6]. The water vapor in outdoor air often results in frost accumulation on the evaporator surface, creating a layer that increases thermal resistance and decreases the heat transfer coefficient [7]. This significantly affects the heat transfer performance and the COP of the heat pump system [8]. Because frost accumulation substantially influences the single-charge driving distance of pure EVs, defrosting techniques for heat pump systems have become a key research area in the automotive and air conditioning sectors and a crucial technology to boost the single-charge driving distance of pure EVs [9].

Defrosting techniques can be classified into active and passive methods [10,11]. Active defrosting techniques include compressor shutdown defrosting, electric heating defrosting, hot water spraying defrosting, hot gas bypass defrosting, and reverse cycle defrosting, etc. [12]. Passive defrosting techniques typically involve the modification of the heat exchanger surface morphology through micro-grooves, anti-freeze coatings, and superhydrophobic coatings to enhance drainage efficiency and reduce frost adhesion [13]. Although passive defrosting techniques exhibit a slower defrost rate than their active counterparts, they focus on preventing frost accumulation at the source and facilitating frost melting [14]. Notably, passive defrosting methods do not require additional systems or extra energy input [15], making them a prominent area of research in recent years.

Several studies have examined the defrosting performance of different passive methods. Amer et al. [16] carried out a comparative analysis of various defrosting techniques, discovering that passive defrosting methods could facilitate frost liquid drainage. Furthermore, superhydrophobic coatings were found to effectively delay frost initiation and exhibited reduced water adhesion during defrosting, offering superior performance compared to hydrophilic and uncoated surfaces. Li et al. [17] conducted periodic frost-defrost experiments on vertical fins coated with hydrophilic and superhydrophobic coatings. They modeled the drainage performance of these surface coatings using dynamic tilt angles. Their results indicated that superhydrophobic surfaces expelled frost in the form of a frost-water mixture during defrosting, thereby reducing the defrosting time by approximately 9.8% compared to hydrophilic surfaces. Consequently, the defrosting capabilities of superhydrophobic surface treatment (SHST) technology proved to be superior to other passive defrosting methods [18].

The defrosting mechanism and performance of SHST technology on heat exchangers have been extensively researched recently. This technology can form a water film on the heat exchanger surface, leading to an approximate reduction of 24% in frost thickness [19]. This reduction led to a decrease in wind resistance and a 44% reduction in defrosting time during heating [20]. Research demonstrated that applying a superhydrophobic coating to the heat exchanger surface decreases condensate formation. This reduced condensate curtailed energy loss due to droplet evaporation and improved defrosting efficiency [21]. In addition, frost accumulation on superhydrophobic surfaces was reported to take twice as long as on untreated surfaces [22]. This effect was largely due to the diminished adhesion of condensate on superhydrophobic surfaces, where droplets often form spherical shapes and display jumping and rolling behaviors [23].

As evidenced by prior research, the SHST techniques have proven effective in enhancing the heat transfer performance of traditional heat exchangers, particularly in large-scale air conditioning systems operating under cold winter conditions. However, there is a research gap concerning the implications of applying the superhydrophobic coating to microchannel heat exchangers (MHEs). MHEs, with their compact structure, lightweight design, and excellent heat transfer capabilities, are well-suited for integration into electric vehicle heat pump systems [24]. It's important to note that the current emphasis of SHST techniques primarily concerns the prevention of frost accumulation, with less investigation into their impact on the cycle performance of heat pumps, such as improving the COP and reducing the compression power.

This study proposes a superhydrophobic surface treatment-based microchannel heat exchanger for application in an electric vehicle heat pump, targeting fin defrosting, flow resistance reduction,

Preprints (www.preprints.org) | NOT PEER-REVIEWED | Posted: 4 August 2023 doi:10.20944/preprints202308.0414.v1



and heat transfer enhancement. Owning to the excellent defrosting effect and heat transfer performance under cold conditions, the COP of the heat pump system and the single-charge driving distance of the electric vehicle are significantly improved by the proposed microchannel heat exchanger with SHST. Based on the computational fluid dynamics (CFD) simulation verified with high accuracies, we investigate the influence of frost accumulation on the heat transfer coefficient and pressure drop. Moreover, we also study the defrosting effect of the superhydrophobic surface on heat transfer performance improvement and flow resistance reduction to elucidate the synergistic mechanism. A dynamic heat pump model utilizing the microchannel heat exchanger with a superhydrophobic surface is developed and validated by experimental results. An experiment is conducted to measure and compare the frost thickness on MHEs with and without SHST. Lastly, we make a fair comparison on the COP, compressor power, fan power, and single-charge driving distance of the heat pump with and without a superhydrophobic surface, highlighting the superiority of SHST techniques.

## 2. Methodology

In this section, the microchannel heat exchanger model is presented to estimate the heat transfer performance and flow resistance, with related parameter settings given. The dynamic heat pump model is established and validated by the existing experiment results.

### *2.1. Microchannel heat exchanger model*

The geometric structure and parameters of the studied microchannel heat exchanger are presented in Figure 1 and Table 1, respectively. Based on these parameters, the heat transfer coefficients and air-side pressure drop can be estimated by the following equations.

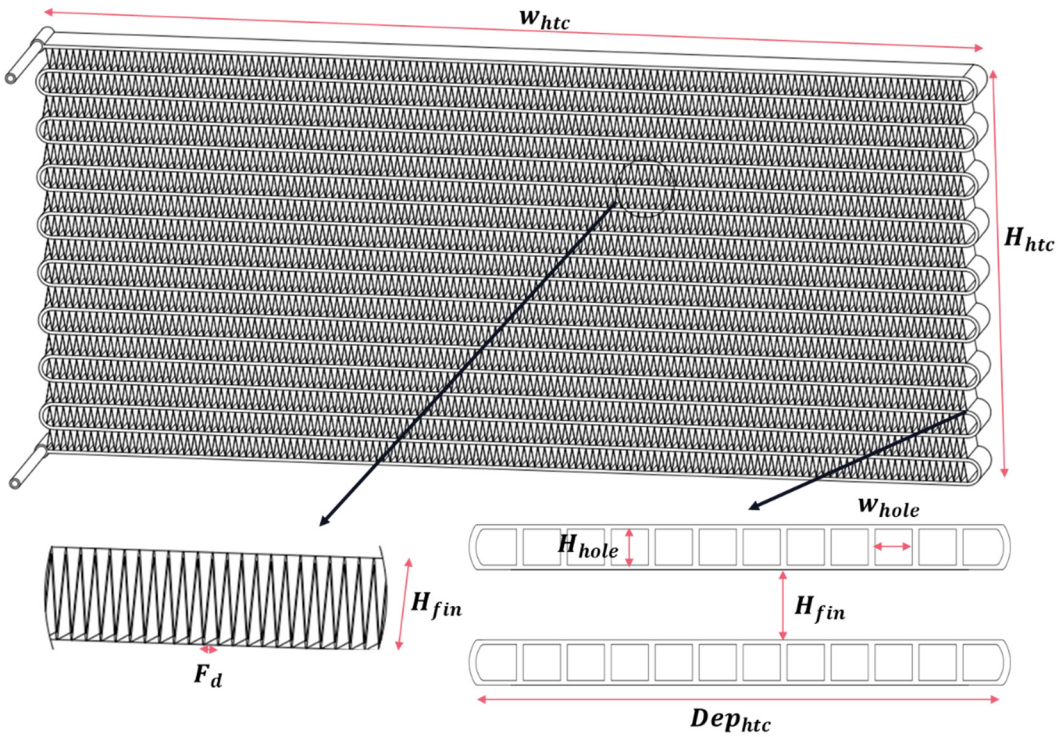


**Figure 1.** The detailed geometric structure of the microchannel heat exchanger.

Preprints (www.preprints.org) | NOT PEER-REVIEWED | Posted: 4 August 2023 doi:10.20944/preprints202308.0414.v1



**Table 1.** The geometric parameters of the studied microchannel heat exchanger.

| Symbol | Meaning | Value |
|---|---|---|
| $H_{fin}$ | distance between flat tubes | 12 mm |
| $H_{hole}$ | port height | 1.6 mm |
| $w_{hole}$ | port width | 2.2 mm |
| $F_d$ | distance between fins | 2 mm |
| $\delta_f$ | fin thickness | 0.15 mm |
| $N_{hole}$ | number of ports per tube | 12 |
| $N_{tube}$ | number of tubes | 10 |
| $w_{htc}$ | HTC width | 548 mm |
| $H_{htc}$ | HTC height | 258 mm |
| $Dep_{htc}$ | HTC depth | 31.2 mm |

The cross-sectional area of the port is calculated by [25]:

$$A_{tube} = (N_{hole} - 2)H_{hole}w_{hole} + 2[\left(w_{hole} - \frac{H_{hole}}{2}\right)H_{hole} + \frac{\pi {H_{hole}}^2}{8}] \quad (1)$$

The perimeter of the port is calculated by:

$$Peri_{tube} = 2(N_{hole} - 2)(H_{hole} + w_{hole}) + (4w_{hole} + \pi H_{hole}) \quad (2)$$

The hydraulic radius of the refrigerant is calculated by:

$$D_r = \frac{4A_{tube}}{Peri_{tube}} \quad (3)$$

The hydraulic radius of the air side is calculated by:

$$D_a = \frac{2F_d H_{fin}}{F_d + 2\sqrt{(F_d - 2)^2 + {H_{fin}}^2}} \quad (4)$$

The heat transfer area at the refrigerant side is calculated by:

$$A_r = 2(N_{hole} - 2)(H_{hole} + w_{hole})N_{tube}w_{htc} + (4w_{hole} + \pi H_{hole})N_{tube}w_{htc} \quad (5)$$

The heat transfer area at the refrigerant side is calculated by:

$$A_a = Dep_{htc}(F_d + 2\sqrt{(F_d - 2)^2 + {H_{fin}}^2})\frac{N_{tube}w_{htc}}{F_d} \quad (6)$$

The heat duties of the condenser and evaporator at the refrigerant side are calculated by:

$$\dot{Q}_r(\tau) = \alpha_r A_r |t_{r,in}(\tau) - t_{r,out}(\tau)| \quad (7)$$

where $\alpha_r$ and $A_r$ refers to the convective heat transfer coefficients and heat transfer area at the refrigerant side, respectively; $t_{r,in}$ and $t_{r,out}$ are the inlet and outlet temperatures on the refrigerant side, respectively.

The heat duties of the condenser and evaporator at the air side are calculated by:

$$\dot{Q}_a(\tau) = \eta_a \alpha_a A_a |t_{a,in}(\tau) - t_{a,out}(\tau)| \quad (8)$$

where $\alpha_a$ and $A_a$ refers to the convective heat transfer coefficients and heat transfer area at the air side, respectively; $t_{a,in}$ and $t_{a,out}$ are the inlet and outlet temperatures at the air side, respectively.

Preprints (www.preprints.org) | NOT PEER-REVIEWED | Posted: 4 August 2023 doi:10.20944/preprints202308.0414.v1



The heat duties of the condenser and evaporator through the heat exchanger wall are calculated by:

$$\dot{Q}_{wall}(\tau) = \lambda_{wall}/\delta_{wall}|t_{wall,int}(\tau) - t_{wall,ext}(\tau)| \quad (9)$$

where $\lambda_{wall}$ and $\delta_{wall}$ refers to the thermal conductivity and thickness of the wall, respectively; $t_{wall,int}$ and $t_{wall,ext}$ are the internal and external temperatures of the wall, respectively. Hence, the overall heat transfer coefficients of the condenser and evaporator are calculated by:

$$U_{tot} = \frac{1}{\frac{1}{\alpha_r}\frac{A_a}{A_r} + \frac{\delta_{wall}}{\lambda_{wall}}\frac{A_a}{A_r} + \frac{1}{\eta_a \alpha_a}} \quad (10)$$

$$\dot{Q}(\tau) = U_{tot} A_a LMTD(\tau) \quad (11)$$

$$LMTD(\tau) = \frac{\left(\Delta T_{a,in}(\tau) - \Delta T_{r,out}(\tau)\right) - \left(\Delta T_{a,out}(\tau) - \Delta T_{r,in}(\tau)\right)}{\ln[\frac{\Delta T_{a,in}(\tau) - \Delta T_{r,out}(\tau)}{\Delta T_{a,out}(\tau) - \Delta T_{r,in(\tau)}}]} \quad (12)$$

where $U_{tot}$ refers to the overall heat transfer coefficients of the condenser and evaporator; $LMTD$ denotes the logarithmic mean temperature difference of the heat exchanger.

The refrigerant-side convective heat transfer coefficient is defined by [26,27]:

$$\alpha_r = \frac{0.023 Re^{0.8} Pr^{0.4} \lambda}{D_r} \quad (13)$$

where $Re$ and $Pr$ refer to the Reynolds number and Prandtl number, respectively.

The air-side convective heat transfer coefficient is defined by [28–30]:

$$\alpha_a = \frac{j \rho_a velo_a C_{p,a}}{Pr^{2/3}} \quad (14)$$

$$Pr = \frac{C_{p,air} \mu_a}{\lambda} \quad (15)$$

$$j = 0.874 Re_a^{-0.716} \quad (16)$$

$$Re_a = \frac{\rho_a velo_a D_a}{\mu} \quad (17)$$

where $\rho_a$ refers to the average air density; $velo_a$ is the mass velocity of the air; $C_{p,a}$ and $\mu_a$ are the specific heat and viscosity of the air; $Nu$ refers to the Nusselt number; $j$ denotes the Colburn $j$-factor, which is a widely used analogy between heat, momentum, and mass transfer.

The air-side pressure drop $\Delta P_a$ is estimated by [30,31]:

$$\Delta P_a = f \frac{{G_a}^2}{2\rho_a} \frac{A_{tot}}{A_{min}} \quad (18)$$

$$f = 0.778 Re_a^{-0.375} \quad (19)$$

where $G_a$ refers to the air mass flux; $A_{min}$ is the minimum free flow area of air through the core; $A_{tot}$ the total heat transfer area in the air side.

Meanwhile, a CFD model was developed to evaluate the effect of air velocity on the microchannel heat exchanger. The laminar model was used to simulate the flow of the air side due

Preprints (www.preprints.org) | NOT PEER-REVIEWED | Posted: 4 August 2023 doi:10.20944/preprints202308.0414.v1



to the low Reynolds number. Detailed governing equations, including mass, energy, and momentum equations, are given as follows [32]:

$$\nabla \cdot \rho \boldsymbol{v} = 0 \tag{20}$$

$$\nabla \cdot \rho \boldsymbol{v}\boldsymbol{v} = -\nabla p + \nabla \cdot (\bar{\bar{\tau}}) + \rho \boldsymbol{g} + \boldsymbol{F} \tag{21}$$

$$\nabla \cdot \left(v(\rho E + p)\right) = \nabla \cdot (\lambda \nabla T) \tag{22}$$

where $\rho$ is the air density; $v$ is the air velocity; $p$ is the pressure; $\bar{\bar{\tau}}$ is the stress tensor; $\boldsymbol{g}$ is the gravitational acceleration; $\boldsymbol{F}$ is the external body forces; $E$ is the energy; $\lambda$ is the thermal conductivity; $T$ is the temperature.

*2.2. Heat pump cycle model*

For the heat pump cycle model, the mass flow rate through the compressor is defined by:

$$m_r(\tau) = \eta_{vol} \frac{V_{comp} n}{60 v_r(\tau)} \tag{23}$$

where $m_r$ is the mass flow rate of the refrigerant; $\eta_{vol}$ is the volumetric efficiency of the compressor; $v_r$ refers to the specific volume of the refrigerant; $V_{comp}$ and n denotes the theoretical displacement and frequency of the compressor.

The power consumed by the compressor is defined by [33]:

$$\dot{W}_{comp}(\tau) = \frac{\dot{m}_r(\tau) \cdot \left(h_{out,ide}(\tau) - h_{in}(\tau)\right)}{\eta_{is,comp} \cdot \eta_{me,comp}} \tag{24}$$

where $\dot{W}_{comp}$ refers to the power consumed by the compressor; $h_{out,ide}$ and $h_{in}$ refer to the ideal specific refrigerant enthalpy at the outlet and the specific refrigerant enthalpy at the inlet; $\eta_{is,comp}$ and $\eta_{me,comp}$ are the isentropic efficiency, and mechanical efficiency, respectively.

The flow in the expansion valve can be regarded as an adiabatic throttling process [34]:

$$h_{ex,in}(\tau) = h_{ex,out}(\tau) \tag{25}$$

$$\dot{m}_r(\tau) = c_{ex} A_{ex} \sqrt{2\rho_r (P_{ex,in}(\tau) - P_{ex,out}(\tau))} \tag{26}$$

where $h_{ex,in}$ and $h_{ex,out}$ refer to the specific enthalpies of the expansion valve inlet and outlet, respectively; $P_{ex,in}$ and $P_{ex,out}$ refer to the pressures of the expansion valve inlet and outlet, respectively; $c_{ex}$ denotes the flow coefficient; $A_{ex}$ is the flow area of the expansion valve.

The power consumed by the fan is defined by:

$$\dot{W}_{fan}(\tau) = \frac{velo_a A_{htc} \Delta P_a(\tau)}{\eta_{fan}} \tag{27}$$

where $\dot{W}_{fan}$ refers to the power consumed by the fan; $A_{fan}$ is the cross-sectional area of the heat exchanger, respectively; $\eta_{fan}$ is the fan efficiency.

The $COP_{sys}$ is the coefficient of performance considering fan power; $COP_{comp}$ is the coefficient of performance only considering compressor power, which are defined by [35,36]:

$$COP_{sys}(\tau) = \frac{Q_c(\tau)}{\dot{W}_{comp}(\tau) + W_{fan}(\tau)} \tag{28}$$

$$COP_{comp}(\tau) = \frac{Q_c(\tau)}{\dot{W}_{comp}(\tau)} \tag{29}$$

Preprints (www.preprints.org) | NOT PEER-REVIEWED | Posted: 4 August 2023 doi:10.20944/preprints202308.0414.v1



*2.3. Model validation*

To verify the feasibility of the established cycle model, the results estimated from the cycle model are compared with those from an experiment on a heat pump applied in an electric coach. The investigated heat pump is designed with a cooling capacity of 23 kW and working fluid of R410a. The width, length, and depth of the external heat exchanger are 1200 mm, 756 mm, and 101.6 mm, respectively, while those of the internal heat exchanger are 681 mm, 378 mm, and 101.6 mm, respectively. The parameter setting of the test conditions for cooling/heating are listed in Table 2.

**Table 2.** Parameter setting of the test conditions.

| | **Cooling test condition** | **Heating test condition** |
|---|---|---|
| Outdoor dry bulb temperature (°C) | 35 | 7 |
| Outdoor wet bulb temperature (°C) | 24 | 6 |
| Mass flow rate of outdoor air (kg/s) | 4.48 | 4.10 |
| Indoor dry bulb temperature (°C) | 27 | 20 |
| Indoor wet bulb temperature (°C) | 19.5 | 15 |
| Mass flow rate of Indoor air (kg/s) | 1.62 | 1.42 |
| Indoor humidity | 0.492 | 0.584 |
| Outdoor humidity | 0.396 | 0.866 |

Tables 3 and 4 present the cooling and heating performance comparison between the experiment and simulation. Under the operating conditions for cooling, the deviations of cooling effect, compressor power, and COP between the experiment and simulation results are 0.43%, 2.38%, and 2.08%. Under the operating conditions for heating, the deviations of cooling effect, compressor power, and COP between the experiment and simulation results are 5.17%, 4.38%, and 8.56%. Hence, the deviations of cooling effect, compressor power, and high-side pressure are lower than 10%, indicating that the established heat pump model is accuracy enough for further study.

**Table 3.** The cooling performance comparison between the experiment and simulation.

| **Item** | **Experiment results** | **Simulation results** | **MAPE** |
|---|---|---|---|
| Cooling effect (kW) | 23.18 | 23.08 | 0.43% |
| Total power consumption (kW) | 9.53 | 9.69 | 1.68% |
| Compressor power (kW) | 6.73 | 6.89 | 2.38% |
| COP | 2.43 | 2.38 | 2.08% |
| High-side pressure (MPa) | 2.92 | 2.97 | 1.71% |
| Low-side pressure (MPa) | 0.98 | 0.87 | 11.22% |

**Table 4.** The heating performance comparison between the experiment and simulation.

| **Item** | **Experiment results** | **Simulation results** | **MAPE** |
|---|---|---|---|
| Cooling effect (kW) | 22.23 | 23.38 | 5.17% |
| Total power consumption (kW) | 8.34 | 8.08 | 3.12% |
| Compressor power (kW) | 5.94 | 5.68 | 4.38% |
| COP | 2.67 | 2.89 | 8.56% |
| High-side pressure (MPa) | 2.58 | 2.525 | 2.13% |
| Low-side pressure (MPa) | 0.98 | 0.87 | 11.22% |

## 3. Air-side flow and heat transfer characteristics with frost growth

The frost growth on the fin surface involves complex heat and mass transfer processes. To simplify the simulation, some assumptions are as follows:

1. the frost distribution is homogeneous and uniform over the heat exchanger;
2. the thermal conductively of the frost ($k_f$) is considered as a function of the frost density as follows [37]:

Preprints (www.preprints.org) | NOT PEER-REVIEWED | Posted: 4 August 2023 doi:10.20944/preprints202308.0414.v1



$$k_f = 1.202 \times 10^{-3} \rho_f^{0.963} \quad (30)$$

where $\rho_f$ is the frost density, which is considered to be 1000 kg/m$^3$ in this work;

3. the heat radiation between the air and frost layer is negligible.

In this CFD simulation, the computational domains include the air domain, frost domain, and fin domain, as shown in Figure 2(a). In an effort to balance efficiency with accuracy in calculations, simulations were conducted using four distinct grid groups, comprising 226570, 283946, 415650, 990106, and 5766436 meshes, respectively. Grid independence was validated by comparing the outlet temperature and inlet pressure of the air domain. Based on the boundary conditions given by Table 5, Figure 2(b) demonstrates that the grid scheme with 990106 meshes achieved independence.

**Table 5.** Boundary conditions.

| Parameter | Value |
|---|---|
| Air-side inlet temperature, $T_a$ | 7 °C |
| Air-side inlet velocity, $v_a$ | 0.5-2.0 m/s |
| Wall temperature, $T_w$ | -5 °C |
| Operating pressure, $P$ | 101 kPa |
| Frosting thickness, $\delta_f$ | 0.2-0.8 mm |

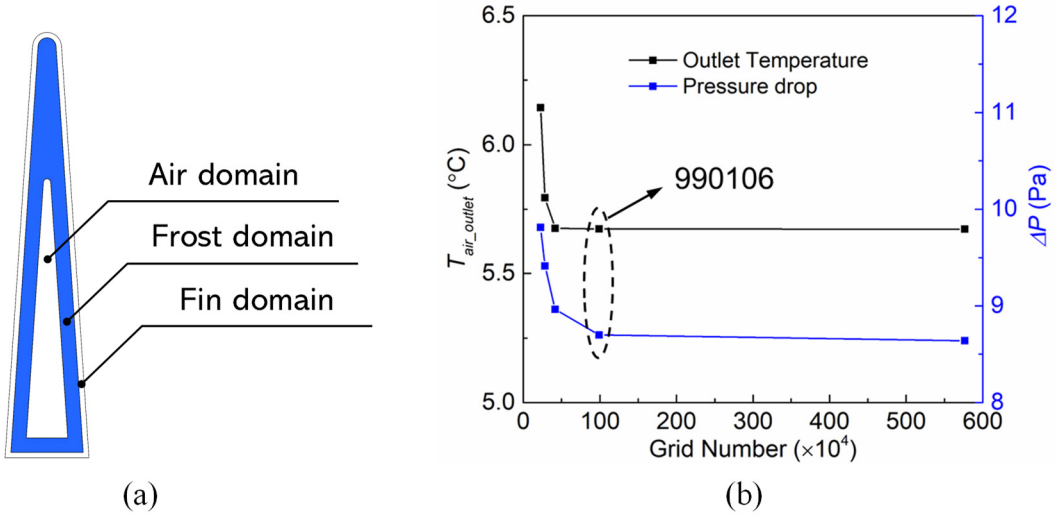


**Figure 2.** (a) Computational domains and (b) grid independence check.

To validate the CFD model, the simulation results were compared with the data published by Siddiqui et al [30]. In that study, the air-side heat transfer and flow performances of a multi-port serpentine cross-flow microchannel heat exchanger were investigated experimentally, and the airflow and heat transfer correlations were derived. It can be seen from Figure 3 that the Nusselt number and pressure drop predicted by the CFD model are in good agreement with the experimental data.

Preprints (www.preprints.org) | NOT PEER-REVIEWED | Posted: 4 August 2023 doi:10.20944/preprints202308.0414.v1



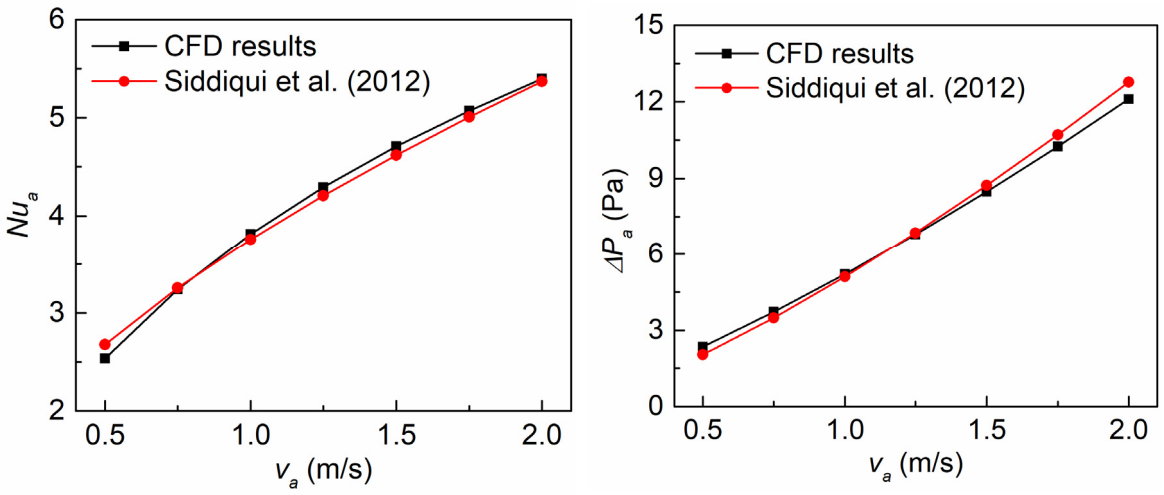


**Figure 3.** Comparison between this work and reference: (a) Nusselt number; (b) pressure drop.

*3.1. The heat transfer coefficients with and without SHST*

Figure 4 depicts the effect of the frost layer thickness on the heat transfer coefficient under different air velocities. In this work, the microchannel heat exchanger without frost growth is considered as a baseline. It can be found that the heat transfer coefficient increases with the increase of air velocity with a power-law relationship, which agrees with the experimental data [30]. For a given air velocity, the heat transfer coefficient decreases as the frost layer thickness increases. The decrease can be attributed to the thermal resistance caused by frost growth. Increasing air velocity improves the heat transfer coefficient, which can relieve the effect of frost growth on heat transfer.

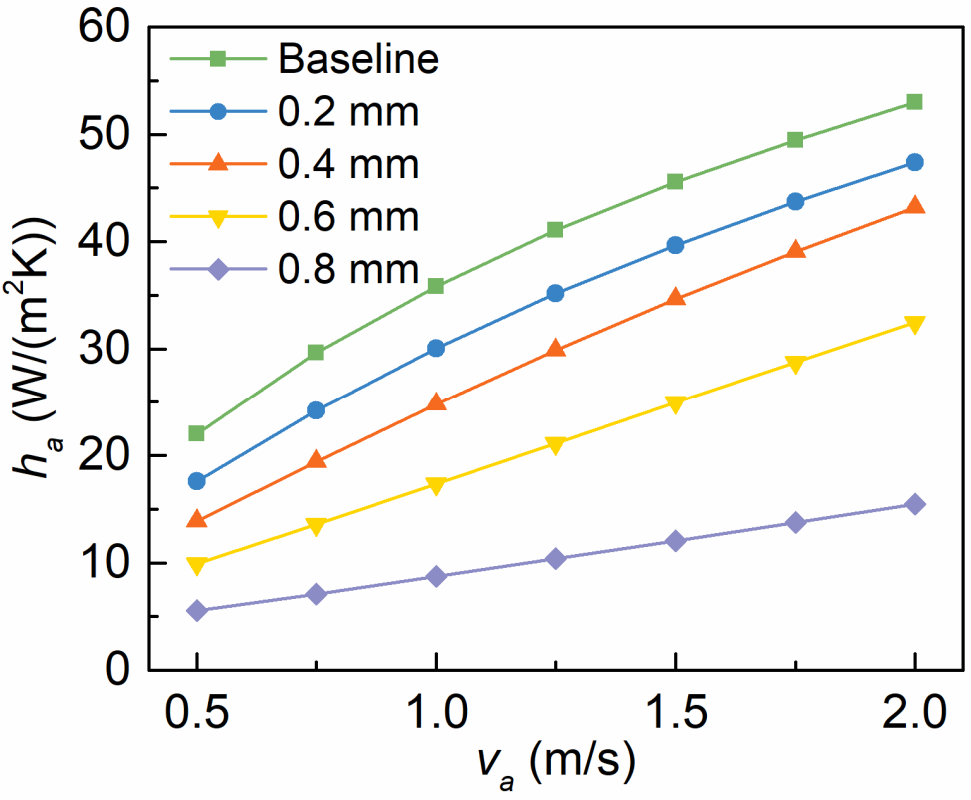


**Figure 4.** Variations of heat transfer coefficients with inlet velocity.

Preprints (www.preprints.org) | NOT PEER-REVIEWED | Posted: 4 August 2023 doi:10.20944/preprints202308.0414.v1



To further understand the effect of frost growth on the air-side heat transfer, a quantitative index ($\alpha_h$) is proposed. The $\alpha_h$ represents the ratio between the heat transfer coefficient of the frost case and that of the baseline (without frost). The frost layer thickness significantly affects the heat transfer characteristics, as shown in Figure 5. The heat transfer coefficient is reduced by about 75% when the frost layer thickness is 0.8 mm. Meanwhile, it can be found from Figure 5 that the effect of the frost growth on the heat transfer coefficient is more significant at a lower velocity.

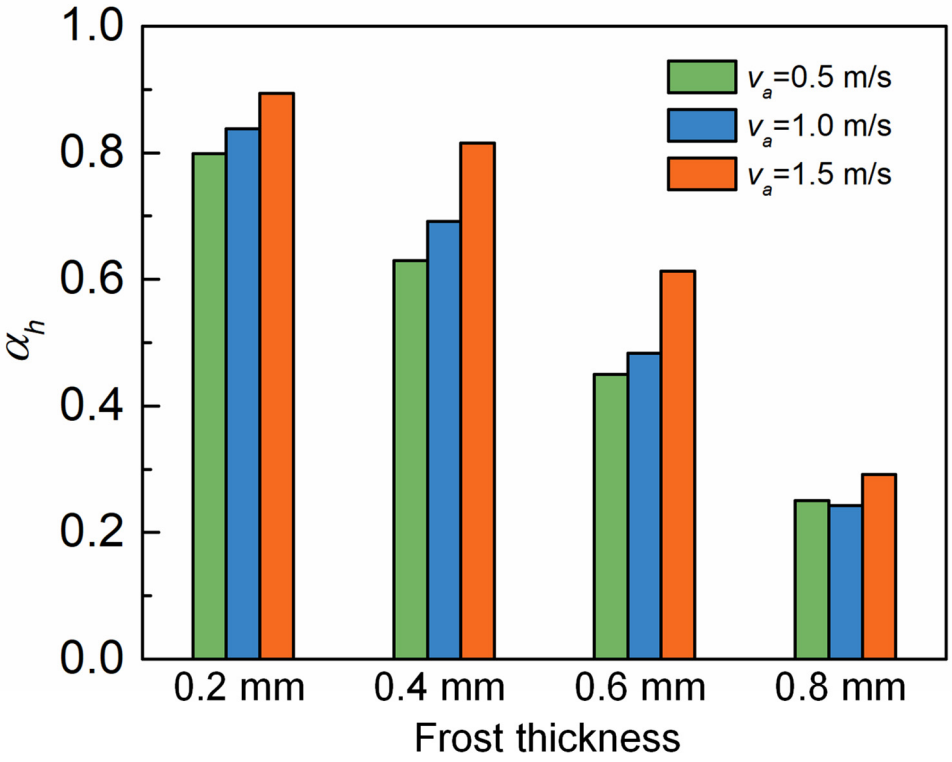


**Figure 5.** The effect of frost growth on the heat transfer coefficients.

*3.2. The pressure drops with and without SHST*

Figure 6 shows the effect of frost layer thickness on the air-side pressure drop between the air-side inlet and the air-side outlet. The air-side pressure drop increases with increasing air velocity in a linear manner, which is consistent with the laminar principle. Meanwhile, the pressure drop increases as the frost layer thickness increases from 0.2 mm to 0.8 mm. The phenomenon can be attributed to the reduced flow area caused by frost growth. It is worth noting that the pressure drop sharply increases when the frost layer thickness is 0.8 mm due to a very narrow flow area, which will significantly increase the pumping power.

Preprints (www.preprints.org) | NOT PEER-REVIEWED | Posted: 4 August 2023 doi:10.20944/preprints202308.0414.v1



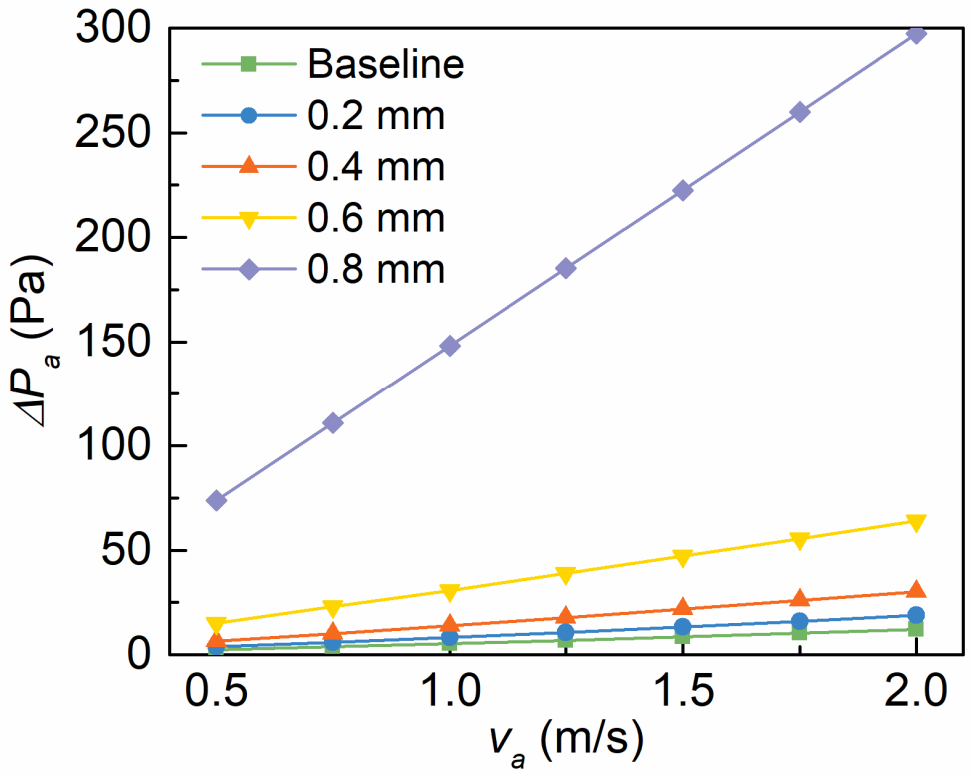


**Figure 6.** Variations of air-side pressure drop with inlet velocity.

Figure 7 illustrates the effect of the frost layer thickness on the air-side pressure drop. For a given air-side inlet velocity of 1.0 m/s, the pressure drop is increased from 1.6 times to 28.4 times with increasing frost layer thickness from 0.2 mm to 0.8 mm compared to the baseline. Meanwhile, the $\alpha_p$ decreases as the air-side inlet velocity increases, especially in the case of a thicker frost layer.

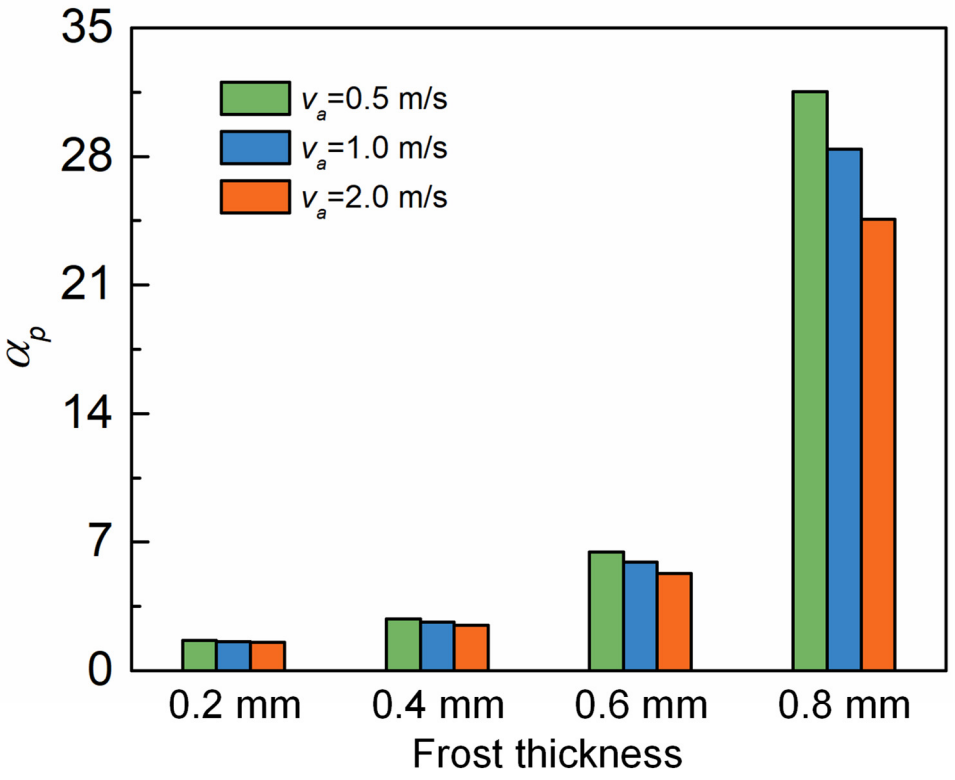

Preprints (www.preprints.org) | NOT PEER-REVIEWED | Posted: 4 August 2023 doi:10.20944/preprints202308.0414.v1



**Figure 7.** The effect of the frost growth on the air-side pressure drop.

## 4. Experiment on microchannel heat exchangers with SHST

To assess the defrosting efficacy of the SHST technology, a microchannel heat exchanger without superhydrophobic coating and another with superhydrophobic coating are situated in a constant temperature and humidity chamber. The internal working fluids are provided by a low-temperature bath to replicate the operating conditions of the evaporator. The air inlet temperature, humidity, and velocity are maintained at 9 °C, 73%, and 1.5 m/s, respectively, while the refrigerant inlet temperature and mass flow rate are kept at -5 °C and 51.75 g/s, respectively. The geometric parameters of the microchannel heat exchangers are given in Table 2. The superhydrophobic coating is sourced from Shenzhen Wei Jing Advanced Materials Co., Ltd, China. The contact angles of copper surfaces with and without SHST are depicted in Figure 8. The contact angle of the surface with superhydrophobic coating exceeds 150 °, which is 51 ° higher than that of the surface without such coating.

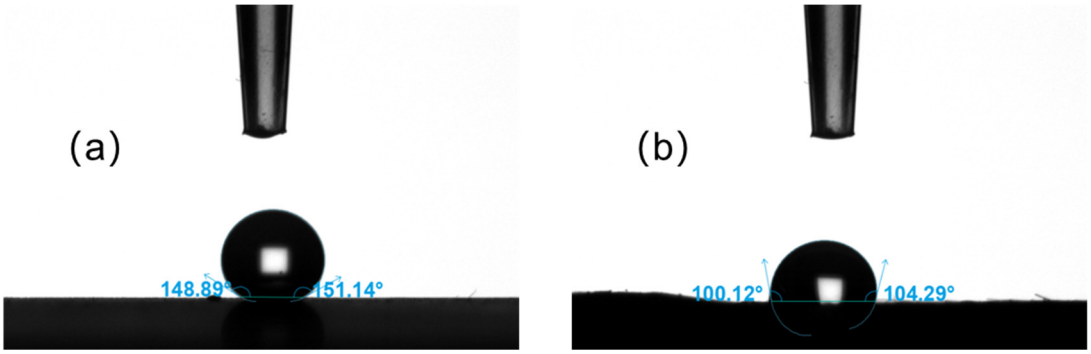


**Figure 8.** The contact angels of (a) surface with SHST, (b) surface with SHST.

Figure 9 portrays the frost thickness of microchannel heat exchangers with and without SHST. At the operating time of 30 min, there is frost accumulation appearing in both the fins with and without superhydrophobic coating. At an operational duration of 30 minutes, frost accumulation is observed on the fins both with and without superhydrophobic coating. The frost thickness of the microchannel heat exchanger with SHST measures approximately 0.4 mm, while that without SHST is about 0.8 mm, signifying that the addition of superhydrophobic coating to the fin surface indeed has a defrosting effect. This observation can be attributed mainly to the spherical shapes formed by droplets and their jumping and rolling behavior due to reduced condensation adhesion on superhydrophobic surfaces, which impedes frost accumulation. When frost thickness reaches 0.8 mm, the formed frost can nearly block the flow areas of the microchannel heat exchanger, explaining the swift decrease in the air-side heat transfer coefficient and pressure drop. The microchannel heat exchanger with SHST demonstrates less frost accumulation than without, enhancing the heat transfer coefficient and improving the cycle performance of heat pumps under cold operating conditions.

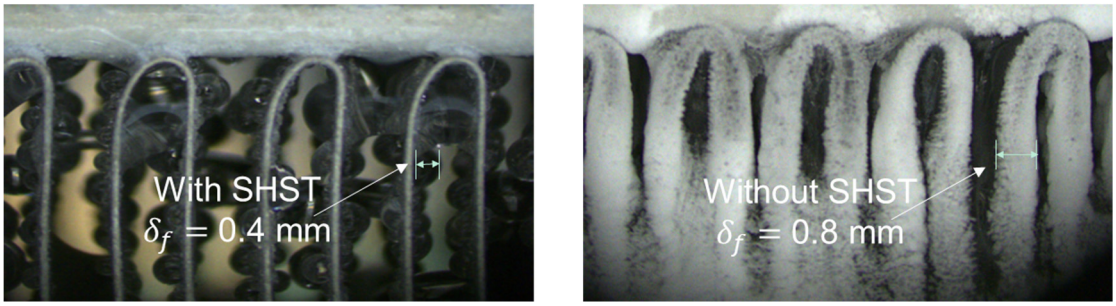


**Figure 9.** The frost thickness of microchannel heat exchange with and without SHST at an operating time of 30 min.

Preprints (www.preprints.org) | NOT PEER-REVIEWED | Posted: 4 August 2023 doi:10.20944/preprints202308.0414.v1



## 5. Cycle performance of heat pump with frost accumulation

In cold operating conditions, frost accumulation can markedly curtail the heating effect, thereby significantly decreasing the COP. This section explores the impact of varying frost thickness on heating effecting, compressor power, fan power, operating pressure, refrigerant flow rate, and COP under various frost thicknesses to ascertain the deterioration in cycle performance induced by frost accumulation. The operating parameters for heating are listed in Table 2.

Figure 10 illustrates the refrigerant mass flow rate with varying frost thickness. A gradual decrease is initially observable in the refrigerant mass flow rate as frost thickness augments, followed by a steep decline. This trend is primarily due to the reduction in the air-side heat transfer rate and an escalation in flow resistance as frost thickness rises, adversely affecting the heat transfer efficiency of the evaporator and diminishing the refrigerant mass flow rate. The degradation of the heat transfer coefficient becomes pronounced when the frost thickness surpasses 0.4 mm, resulting in a sharp decrease in the refrigerant mass flow rate.

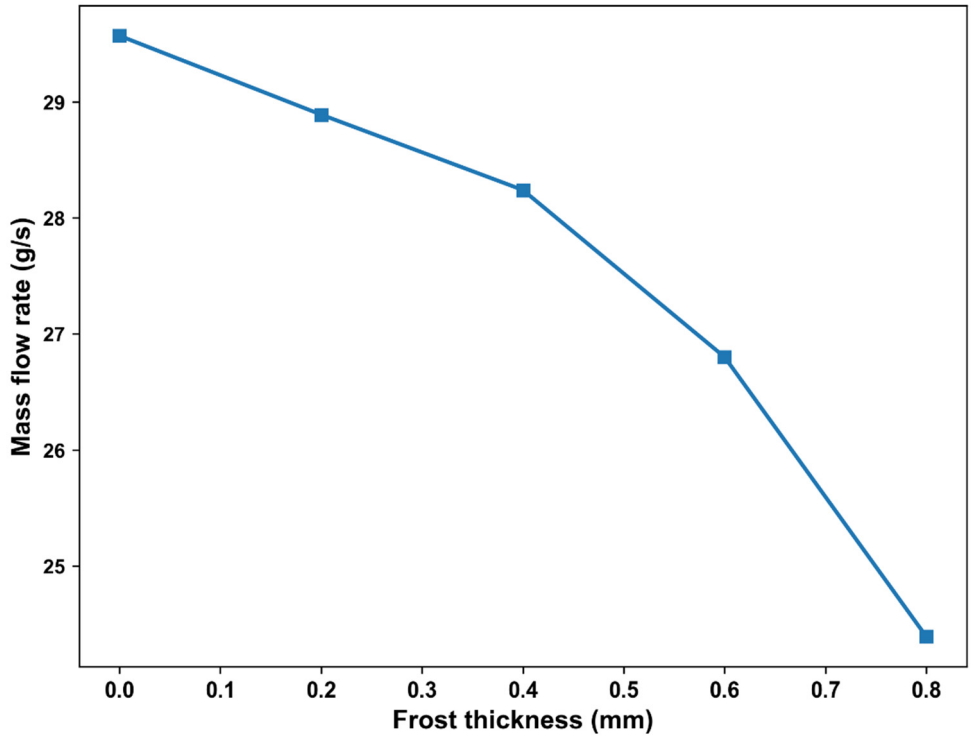


**Figure 10.** Variation of refrigerant mass flow rate with frost accumulation.

Figure 11 demonstrates the changes in the high-side pressure $P_{high}$ and low-side pressure $P_{low}$ of the heat pump system in response to variations in frost thickness. An increase in frost thickness results in a decrease in both high-side and low-side pressures, attributable to the reduced heat transfer coefficient, which consequently leads to a decrease in evaporator temperature and thus a reduced low-side pressure. The refrigerant temperature at the compressor outlet also drops due to a lower inlet temperature, causing a decrease in the condenser temperature and hence a lower high-side pressure. Thus, frost accumulation induces a drop in heat transfer efficiency, resulting in a lower refrigerant mass flow rate and operating pressures.

Preprints (www.preprints.org) | NOT PEER-REVIEWED | Posted: 4 August 2023 doi:10.20944/preprints202308.0414.v1



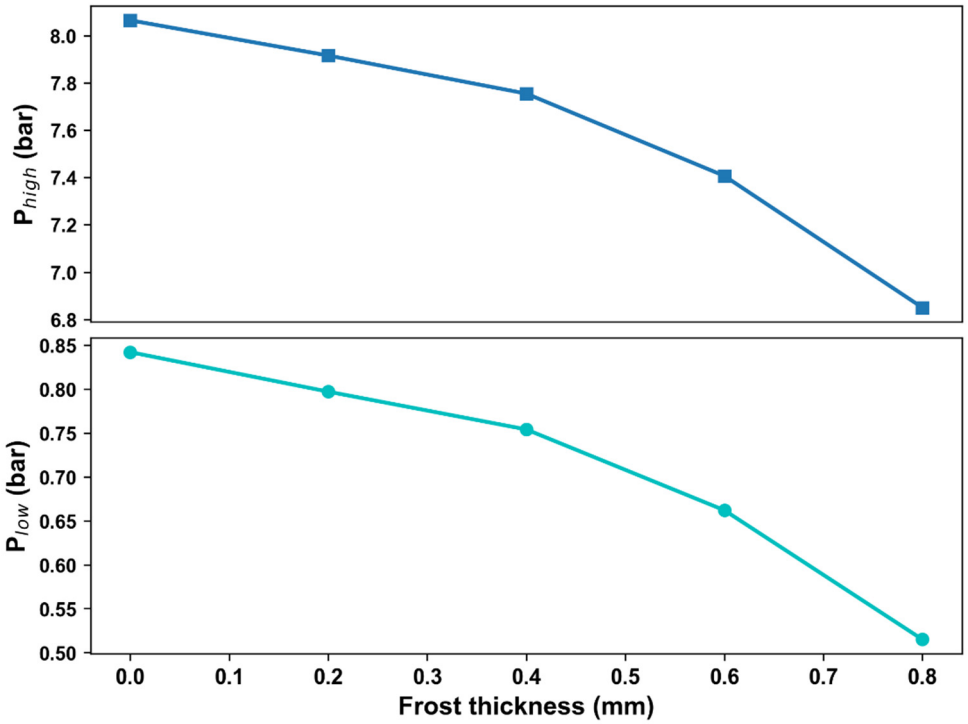


**Figure 11.** High-side pressure $\boldsymbol{P_{high}}$ and low-side pressure $\boldsymbol{P_{low}}$ of the heat pump system with frost accumulation.

Figure 12 reveals the impact of frost thickness on the heating effecting, compressor power, and fan power. With the increase in frost thickness, a decline in the heating effect is observed, primarily attributed to a lower refrigerant mass flow rate and a lower high-side pressure, resulting in a smaller refrigerant enthalpy change in the indoor heat exchanger. With an increase in frost thickness from 0 to 0.8 mm, the heating effect declines from 3.97 to 1.82 kW. The compression power also declines as frost forms, caused by a lower refrigerant mass flow rate. When frost thickness exceeds 0.4 mm, the heating effect and compression power decrease steeply, implying that frost thickness should be restrained to 0.4 mm during operation to maintain an adequate heating effect. Figure 13 presents the effect of frost accumulation on the fan power and pressure drop. As frost thickness rises, so does the pressure drop, necessitating an increased fan power to counteract the flow resistance. A significant increase in fan power from 0.037 kW to 0.13 kW is observed when the frost thickness increases from 0.6 mm to 0.8 mm, primarily due to the abrupt increase in flow resistance and pressure drop.

Preprints (www.preprints.org) | NOT PEER-REVIEWED | Posted: 4 August 2023 doi:10.20944/preprints202308.0414.v1



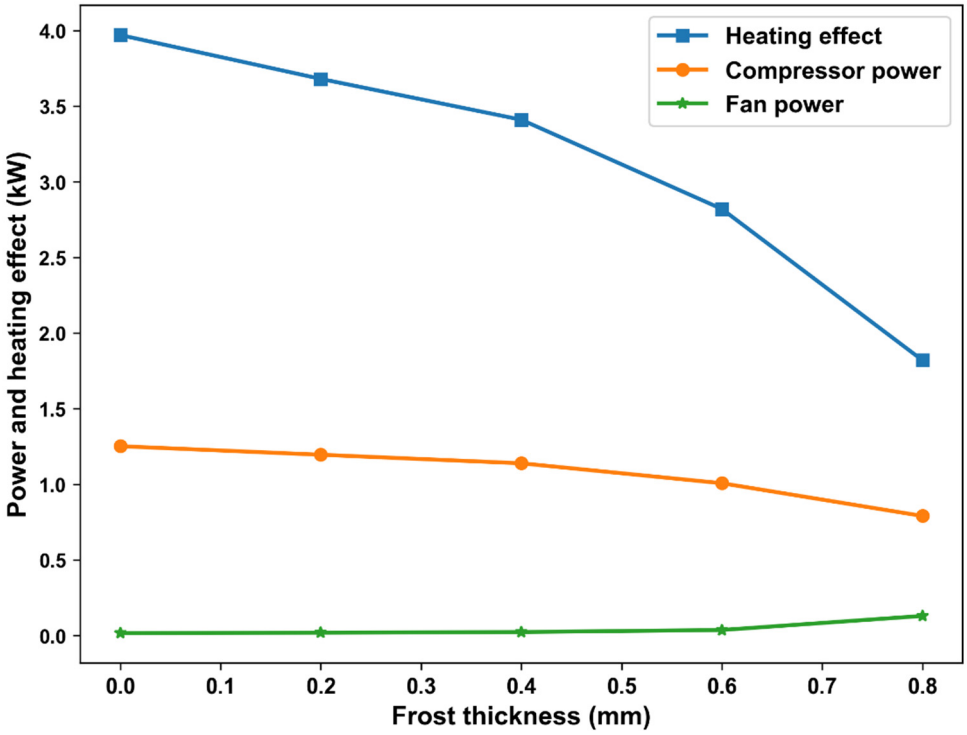


**Figure 12.** Variation of heating effecting, compressor power, and fan power with frost accumulation.

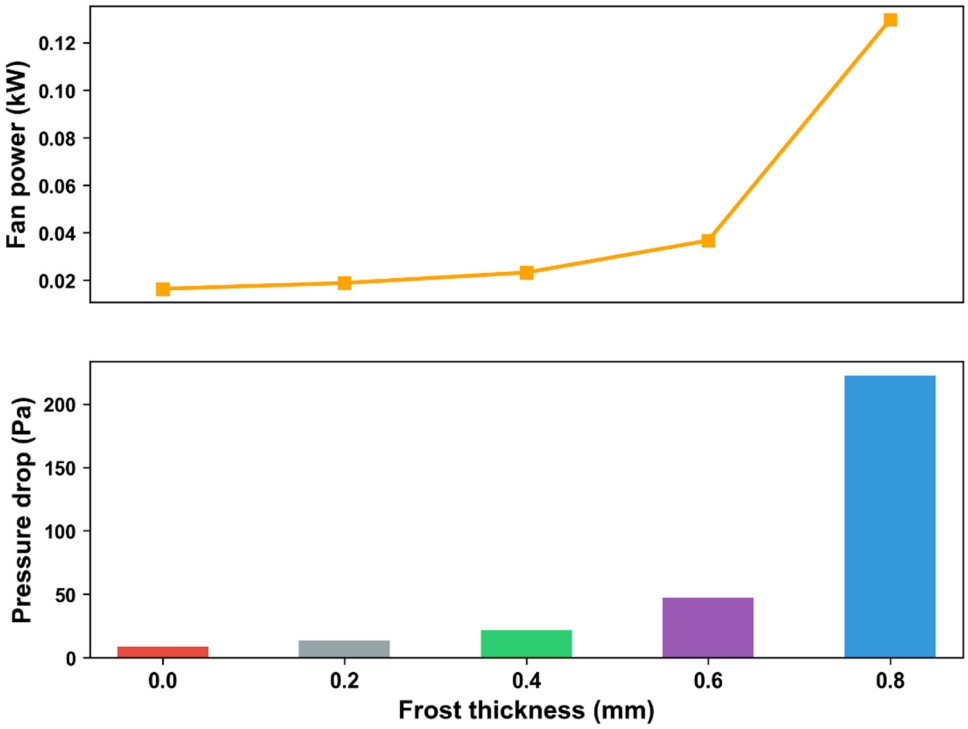


**Figure 13.** Variation of fan power and pressure drop with frost accumulation.

Figure 14 represents the compressor COP and system COP under various frost thicknesses. With an increase in frost thickness from 0 to 0.8 mm, the system COP (factoring in both compression power and fan power) declines from 3.17 to 2.30, while the compressor COP, which only considers compression power, reduces from 3.13 to 1.97. Despite the fact that both the heating effect and compression power decrease as frost thickness escalates, a continuous decrease in both the compressor COP and system COP is observed, owing to the more pronounced decrease in the heating

Preprints (www.preprints.org) | NOT PEER-REVIEWED | Posted: 4 August 2023 doi:10.20944/preprints202308.0414.v1



effect compared to the compression power. Furthermore, the system COP decline is further propelled by the increased pressure drop and fan power. A rise in frost thickness causes an increase in fan power, thus amplifying the discrepancy between the system COP and compressor COP. When the frost thickness is reduced to 0.8 mm, the system COP shrinks to 1.97. This significant reduction potentially elevates power consumption for heating, consequently reducing the single-charge driving distance.

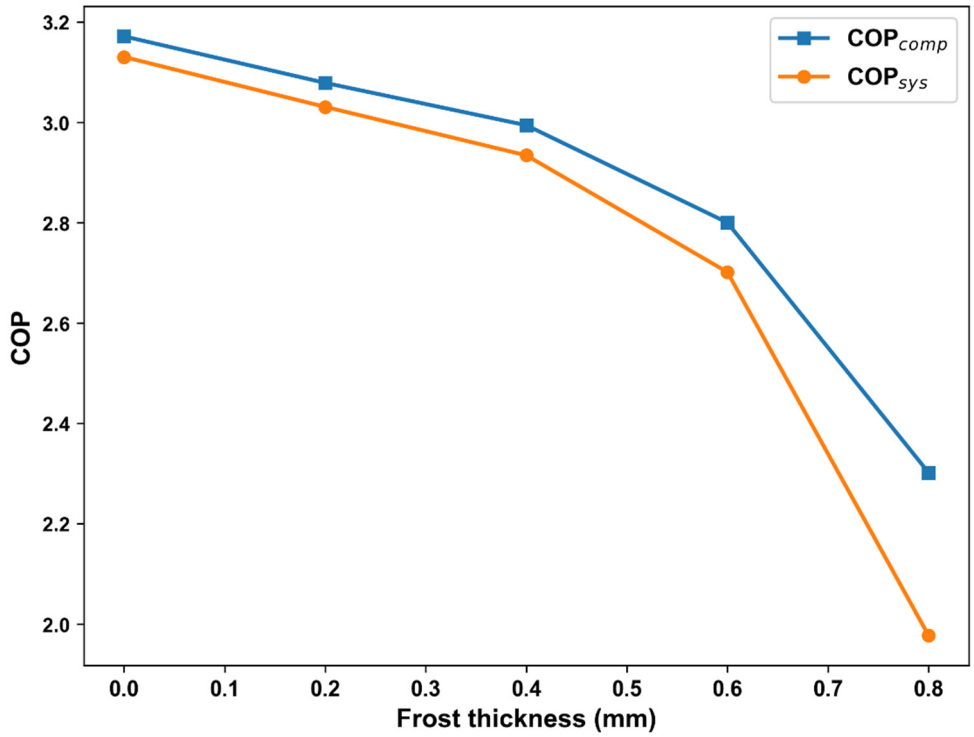


**Figure 14.** Variation of compressor COP and system COP with frost accumulation.

## 6. Performance comparison of EVs using different heating methods

Using an EV with a battery capacity of 60 kWh and a driving velocity of 50 km/h as a benchmark, the COP, power consumption for heating, EV power consumption, and single-charge driving distance of four heating methods, including heat pump with ideal SHST, heat pump with SHST, heat pump without SHST, and traditional positive temperature coefficient (PTC) heating, are comparably analyzed. The 'heat pump with ideal SHST' means that the applied superhydrophobic coating can completely eliminate frost accumulation, representing the ideal defrosting effect achievable by SHST technology. The PTC heating method, commonly utilized for heating EVs in cold winters, has a notably low COP, assumed to be 0.95 in this study. The cycle performance of heat pump with ideal SHST, heat pump with SHST, and heat pump without SHST methods are evaluated based on established models of heat pumps and microchannel heat exchangers.

As indicated in Figure 15 (a), the COP of heat pump without superhydrophobic coating is 1.98 due to the cycle performance deterioration under cold conditions. However, with the application of SHST, the COP of the heat pump increases to 2.93, indicating that the power consumption of heat pump with SHST is 48.7% less than that of heat pump without SHST. Furthermore, the COP of heat pump with an ideal superhydrophobic coating reaches 3.13, illustrating the potential of superhydrophobic coating in preventing cycle performance deterioration. The SHST also facilitates enhanced cooling cycle performance by promoting condensate drainage and reducing the liquid film area on the fins. Under the cooling conditions specified in Table 2, the COP for cabin cooling reaches 2.72. Figure 15 (b) indicates that the power consumption for heating is in the following order: heat pump with ideal SHST (1.60 kW) < heat pump with SHST (1.70 kW) < heat pump without SHST (2.53 kW) < PTC heating (5.36 kW). This order highlights that a higher COP corresponds to lower energy

Preprints (www.preprints.org) | NOT PEER-REVIEWED | Posted: 4 August 2023 doi:10.20944/preprints202308.0414.v1



consumption. The power consumption by the EV follows the same pattern as that for heating. At a driving speed of 50 km/h, an EV equipped with SHST consumes 9.17 kWh per hour, 38.8% greater than traditional PTC heating. Lastly, a comparative analysis on the single-charge driving distances of the four heating methods is conducted in Figure 15 (d). The single-charge driving distance of heat pump with SHST reaches 327.27 km, which is 8.99% longer than that of heat pump without SHST and 28.0% longer than that of traditional PTC heating. Consequently, the application of SHST technology can significantly improve the cycle performance of heat pumps and augment the single-charge driving distance of EVs.

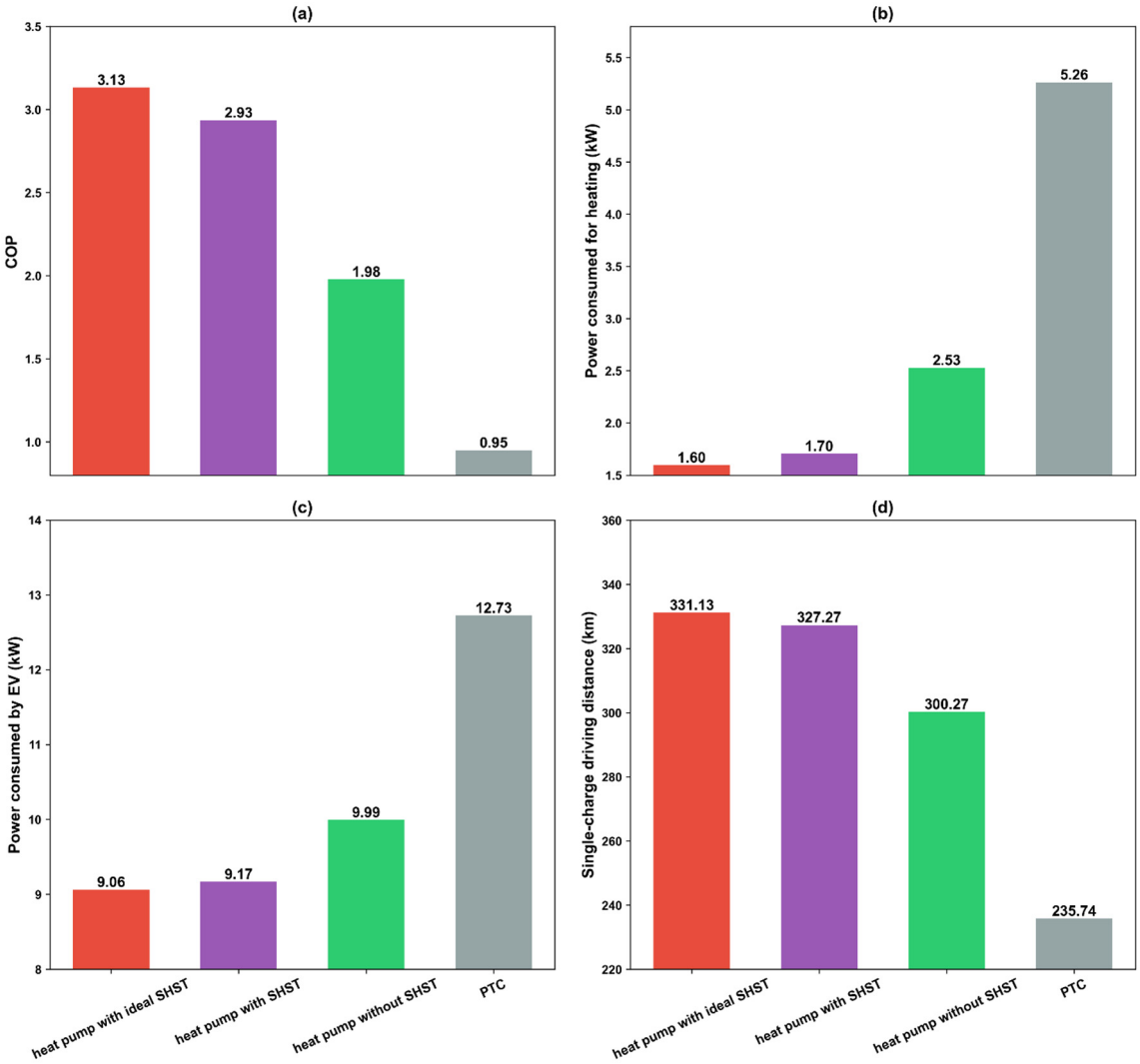


**Figure 15.** Performance comparison of EVs using different heating methods: (a) COP, (b) power consumed for heating, (c) power consumed by EV, and (d) single-charge driving distance.

## 7. Conclusions

This work investigates a microchannel heat exchanger (MHE) with superhydrophobic surface treatment (SHST) as an evaporator to overcome the heating effect attenuation problem of heat pumps in electric vehicles (EVs), which is caused by frost accumulation under cold conditions. By integrating the MHE model, CFD simulation, and dynamic heat pump model verified with high accuracies, the adverse effecting of the frost accumulation on air-side heat transfer, air-side flow resistance, and heat pump cycle performance are investigated. An experiment was conducted to compare the frost thickness on MHEs with and without SHST. Furthermore, the performance of different heating methods in EVs is comparably analyzed to elucidate the advantages of SHST technology. Key findings of the research include:

(1) The validated CFD model demonstrates that frost growth significantly affects the heat transfer characteristics of MHEs. When the frost layer thickness is 0.8 mm at a given air-side velocity of 1.0 m/s, the air-side heat transfer coefficient can be reduced by about 75%, and the air-side pressure drop sharply increases by 28.4 times.

(2) As frost thickness increases from 0 to 0.8 mm, the heating output decreases from 3.97 to 1.82 kW and the system COP declines from 3.17 to 2.30. When frost thickness exceeds 0.4 mm, both the heating output and COP decrease dramatically.

(3) After 30 minutes of operation, the frost thickness on an MHE treated with SHST is approximately 0.4 mm, while an MHE without SHST attains a frost thickness of about 0.8 mm. These results confirm the defrosting capability of superhydrophobic coatings. Once the frost thickness reaches 0.8 mm, the frost can obstruct the flow areas of the MHE, leading to a rapid decrease in the air-side heat transfer coefficient and COP.

(4) With the MHE using SHST, the heat pump system achieves a heating COP of 2.93 and a cooling COP of 2.72. Compared to an untreated MHE, the flow resistance and power consumption of the proposed system is reduced by 90.1% and 48.7%, owing to the defrosting capability of the SHST. Additionally, the single-charge driving distance of an heat pump with SHST extends to 327.27 km, which is 8.99% longer than an heat pump without SHST and 28.0% longer than a traditional positive temperature coefficient heater.

This work is expected to explore new avenues for developing innovative heating solutions in winter conditions, a critical step toward facilitating more effective and sustainable electric vehicles in support of carbon neutrality.

**Acknowledgments:** This study is supported by the Central Government Fund for Guiding Local Scientific and Technological Development under Shenzhen Virtual University Park, Shenzhen Science and Technology Innovation Committee (Project number: 2021Szvup125), and the Research Grants Council of Hong Kong (Project number: CityU 11212620, CityU 11215621).

## Nomenclature

| | |
|---|---|
| $A$ | area, m² |
| $C_p$ | heat capacity, kJ/(kg·K) |
| $D$ | hydraulic radius, m |
| $H$ | height, m |
| $h$ | specific enthalpies, kJ/kg |
| $\dot{m}$ | mass flow rate, kg/s |
| $P$ | pressure, kPa |
| $\dot{Q}$ | heat transfer rate, kW |
| $D$ | hydraulic radius, m |
| $t$ | temperature, °C |
| $U$ | overall heat transfer coefficient, W/(m²·K) |
| $V$ | Volume, m³ |
| $\dot{W}$ | work, kW |
| $\alpha$ | convective heat transfer coefficient, W/(m²·K) |
| $\rho$ | density, kg/m³ |
| $\mu$ | viscosity, Pa·s |
| $\eta$ | efficient |
| $\lambda$ | thermal conductivity, W/(m·K) |
| $\delta$ | thickness, m |

## Abbreviations

| | |
|---|---|
| COP | coefficient of performance |
| CFD | computational fluid dynamics |
| EV | electric vehicle |
| MAPE | mean absolute percentage error |
| MHE | microchannel heat exchanger |
| PTC | positive temperature coefficient |

SHST superhydrophobic surface treatment

## Subscripts

| | |
|---|---|
| a | air side |
| comp | compressor |
| dis | discharge |
| ex | expansion valve |
| ext | external |
| fan | fan |
| htc | heat exchanger |
| in | inlet |
| int | internal |
| is | isentropic |
| me | mechanical |
| out | outlet |
| r | refrigerant |
| sys | system |

## References


1. Z. Li, A. Khajepour, J. Song. A comprehensive review of the key technologies for pure electric vehicles. Energy. 2019. 182. 824-839.
2. S.Z. Rajper, J. Albrecht. Prospects of electric vehicles in the developing countries: a literature review. Sustainability. 2020. 12. 1906.
3. F. Bode, N.V. Burnete, L. Fechete Tutunaru, I. Nastase. Improving Electric Vehicle Range and Thermal Comfort through an Innovative Seat Heating System. Sustainability. 2023. 15. 5534.
4. Z. Zhang, J. Wang, X. Feng, L. Chang, Y. Chen, X. Wang. The solutions to electric vehicle air conditioning systems: A review. Renewable and Sustainable Energy Reviews. 2018. 91. 443-463.
5. Z. Qi. Advances on air conditioning and heat pump system in electric vehicles–A review. Renewable and Sustainable Energy Reviews. 2014. 38. 754-764.
6. Q. Peng, Q. Du. Progress in heat pump air conditioning systems for electric vehicles—a review. Energies. 2016. 9. 240.
7. P. Jakończuk, K. Śmierciew, J. Gagan, D. Butrymowicz. Image-Analysis-Based Approach for Identification of Air Cooler Heat Transfer Degradation during Frosting Process. Sustainability. 2022. 14. 13731.
8. W. Li, Y. Liu, R. Liu, D. Wang, J. Shi, Z. Yu, et al. Performance evaluation of secondary loop low-temperature heat pump system for frost prevention in electric vehicles. Applied Thermal Engineering. 2021. 182. 115615.
9. A.J. Mahvi, K. Boyina, A. Musser, S. Elbel, N. Miljkovic. Superhydrophobic heat exchangers delay frost formation and enhance efficency of electric vehicle heat pumps. International Journal of Heat and Mass Transfer. 2021. 172. 121162.
10. D. Badri, C. Toublanc, O. Rouaud, M. Havet. Review on frosting, defrosting and frost management techniques in industrial food freezers. Renewable and Sustainable Energy Reviews. 2021. 151. 111545.
11. B. Yang, X. Zhu, M. Liu, Z. Lv. Review on the application of machine vision in defrosting and decondensation on the surface of heat exchanger. Sustainability. 2022. 14. 11606.
12. M. Song, S. Deng, C. Dang, N. Mao, Z. Wang. Review on improvement for air source heat pump units during frosting and defrosting. Applied energy. 2018. 211. 1150-1170.
13. Y. Gurumukhi, S. Chavan, S. Sett, K. Boyina, S. Ramesh, P. Sokalski, et al. Dynamic defrosting on superhydrophobic and biphilic surfaces. Matter. 2020. 3. 1178-1195.
14. J. Liu, M. Kappl, H.-J. Butt. Toward passive defrosting with heterogeneous coatings. Matter. 2020. 3. 981-983.
15. A. Foster, R. Campbell, T. Davies, J. Evans. A novel passive defrost system for a frozen retail display cabinet with a low evaporator. The 24th IIR International Congress of Refrigeration. International Institute of Refrigeration2015.
16. M. Amer, C.-C. Wang. Review of defrosting methods. Renewable and Sustainable Energy Reviews. 2017. 73. 53-74.
17. F. Li, S. Wu, Z. Ma, R. Zhao, D. Huang. Effect of surface coating on defrosting water drainage characteristics of vertical-fin microchannel frosting evaporator. Applied Thermal Engineering. 2022. 208. 118220.

18. J.B. Boreyko, B.R. Srijanto, T.D. Nguyen, C. Vega, M. Fuentes-Cabrera, C.P. Collier. Dynamic defrosting on nanostructured superhydrophobic surfaces. Langmuir. 2013. 29. 9516-9524.
19. J. Shin, A.V. Tikhonov, C. Kim. Experimental study on frost structure on surfaces with different hydrophilicity: density and thermal conductivity. J Heat Transfer. 2003. 125. 84-94.
20. M.A. Kadhim, N. Kapur, J.L. Summers, H. Thompson. Experimental and theoretical investigation of droplet evaporation on heated hydrophilic and hydrophobic surfaces. Langmuir. 2019. 35. 6256-6266.
21. F. Wang, C. Liang, M. Yang, C. Fan, X. Zhang. Effects of surface characteristic on frosting and defrosting behaviors of fin-tube heat exchangers. Applied Thermal Engineering. 2015. 75. 1126-1132.
22. Z. Liu, Y. Gou, J. Wang, S. Cheng. Frost formation on a super-hydrophobic surface under natural convection conditions. International Journal of Heat and Mass Transfer. 2008. 51. 5975-5982.
23. A. Kim, C. Lee, H. Kim, J. Kim. Simple approach to superhydrophobic nanostructured Al for practical antifrosting application based on enhanced self-propelled jumping droplets. ACS applied materials & interfaces. 2015. 7. 7206-7213.
24. M.G. Khan, A. Fartaj. A review on microchannel heat exchangers and potential applications. International journal of energy research. 2011. 35. 553-582.
25. Z.-g. Qi, J.-p. Chen, Z.-j. Chen. Parametric study on the performance of a heat exchanger with corrugated louvered fins. Applied thermal engineering. 2007. 27. 539-544.
26. F.W. Dittus. Heat transfer in automobile radiators of the tubular type. Univ of California Pub, Eng. 1930. 2. 443-461.
27. Y. Sui, C. Zhai, H. Lin, W. Wu. How to rationally screen refrigerant/ionic liquids for thermal cooling: A multi-criteria approach based on machine learning. Energy Conversion and Management. 2023. 282.
28. M.-H. Kim, C.W. Bullard. Air-side performance of brazed aluminum heat exchangers under dehumidifying conditions. International Journal of refrigeration. 2002. 25. 924-934.
29. N.A. Qasem, S.M. Zubair. Compact and microchannel heat exchangers: A comprehensive review of air-side friction factor and heat transfer correlations. Energy conversion and management. 2018. 173. 555-601.
30. F.A. Siddiqui, E.S. Dasgupta, A. Fartaj. Experimental investigation of air side heat transfer and fluid flow performances of multi-port serpentine cross-flow mesochannel heat exchanger. International journal of heat and fluid flow. 2012. 33. 207-219.
31. J. Boeng, A.A. Marcon, C.J. Hermes. Air-side heat transfer and pressure drop characteristics of microchannel evaporators for household refrigerators. International Journal of Heat and Mass Transfer. 2020. 147. 118913.
32. A. Fluent. ANSYS Fluent Theory Guide, Release 18.0. Ansys. Inc: Canonsburg, PA, USA. 2017.
33. Y. Sui, Z. Ding, C. Zhai, H. Lin, W. Wu. Crystallization-free and low-cost deep eutectic solvents for absorption thermal battery utilizing ultra-low-grade energy. Energy Conversion and Management. 2023. 284. 116984.
34. Y.R. Sui, C. Zhai, W. Wu, M.K.H. Leung. Multi-scale Computer-aided molecular design of Ionic liquid for absorption heat transformer based on Machine learning. Energy Conversion and Management. 2022. 261.
35. Y. Sui, W. Wu. Ionic liquid screening and performance optimization of transcritical carbon dioxide absorption heat pump enhanced by expander. Energy. 2023. 263.
36. L.-L. Shao, L. Yang, C.-L. Zhang. Comparison of heat pump performance using fin-and-tube and microchannel heat exchangers under frost conditions. Applied Energy. 2010. 87. 1187-1197.
37. D.-K. Yang, K.-S. Lee, S. Song. Modeling for predicting frosting behavior of a fin–tube heat exchanger. International journal of heat and mass transfer. 2006. 49. 1472-1479.